Communications Chemistry

https://doi.org/10.1038/s42004-026-01976-x

Article in Press

Curvature-induced vitrification and polymorphism in corannulene

Received: 1 August 2025

Accepted: 5 March 2026

Cite this article as: Gaboardi, M., Di Lisio, V., Braunewell, B. *et al.* Curvature-induced vitrification and polymorphism in corannulene. *Commun Chem* (2026). https://doi.org/10.1038/s42004-026-01976-x

Mattia Gaboardi, Valerio Di Lisio, Balthasar Braunewell, Jay Siegel, Daniele Cangialosi & Felix Fernandez-Alonso

Curvature-induced vitrification and polymorphism in corannulene

Mattia Gaboardi[1,2,3], Valerio Di Lisio[1,4], Balthasar Braunewell[1], Jay Siegel[5], Daniele Cangialosi[1,4*], Felix Fernandez-Alonso[1,4,6*]

[1]Centro de Física de Materiales (CFM-MPC), CSIC-UPV/EHU, Paseo de Manuel Lardizabal 5, Donostia - San Sebastian, 20018, Gipuzkoa, Spain.

[2]Physics Department, University of Rome Tor Vergata, via della Ricerca Scientifica 1, Roma, 00133, Lazio, Italy.

[3]INFN – Rome Tor Vergata, via della Ricerca Scientifica 1, Roma, 00133, Lazio, Italy.

[4]Donostia International Physics Center, DIPC, Paseo de Manuel Lardizabal 4, Donostia - San Sebastian, 20018, State, Spain.

[5]Department of Chemistry, University of Hong Kong, Pokfulam Road, Hong Kong SAR, China.

[6]IKERBASQUE, Basque Foundation for Science, Plaza Euskadi 5, Bilbao, 48009, Bizkaia, Spain.

*Corresponding author(s). E-mail(s): daniele.cangialosi@ehu.eus; felix.fernandez@ehu.eus;

Contributing authors: mattia.gaboardi@uniroma2.it; valerio.dilisio@dipc.org; bjohann001@ikasle.ehu.eus; siegeljsx@gmail.com;

Abstract

Polymorphism in polyarenes significantly impacts their applications, yet remains underexplored in curved species like corannulene. To this end, we utilised fast scanning calorimetry and X-ray diffraction to explore its stability regimes. Unlike its flat counterpart perylene, corannulene exhibits a glass transition at $\boldsymbol{T}_{\mathrm{g}}$ =323 K when cooled from the melt at rates exceeding -500 K s^{-1}. Upon heating, three thermal events at *ca.* 380, 430, and 500 K reveal hitherto unknown polymorphs. Diffraction data link these transitions to well-defined and thermally activated rotations within the crystal, inducing a sharp density decrease matching

T_g. These changes are accompanied by abnormal atomic displacement parameters. Unlike flat polyarenes of a similar molecular size, the diffraction data also provide strong evidence that this solid ought to be regarded as two distinctly different materials below and above T_g. Altogether, our findings bring to the fore the unanticipated complexity underpinning the structure and thermodynamic response of solid corannulene, the simplest geodesic polyarene.

Keywords: corannulene, polymorphism, Polycyclic Aromatic Hydrocarbons, geodesic polyarenes, fast scanning calorimetry, single-crystal synchrotron diffraction, vitrification

1 Introduction

Polymorphism is a key phenomenon across a growing number of fields, from crystal engineering to the development of pharmaceutical drugs. Changes in atomic and molecular packing in the solid state can lead to drastic changes in properties and, as such, the emergence of a polymorph is typically accompanied by a structural transformation to a different crystallographic space group. However, polymorphism can also be the result of more nuanced disorder-driven rearrangements within the same lattice symmetry [1]. In this context, polymorphism has been observed in flat Polycyclic Aromatic Hydrocarbons (PAHs) such as perylene [2, 3], coronene [4] or pentacene [5]. The curved PAH corannulene ($C_{20}H_{10}$, hereafter CA) remains an exception to the above as the simplest 'geodesic polyarene' [6]. To date, only one solid-state structure (so-called α-phase) has been observed in the bulk, although two-dimensional polymorphs have been produced on surfaces [7]). Crystallographic studies tell us that CA conforms to the $P2_1/c$ (Z=8) space group [8, 9]. The curvature of CA gives rise to rather unique electronic properties [10, 11] reminiscent to those of fullerenes [12]. These similarities have been explored to render CA as an attractive platform for applications that rely on the presence of highly charged electronic states, such as those found in alkali-metal salts [13–18] and complexes [19–21]. Additionally, the biological activity of CA in living organisms has also been investigated [22]. Owing to its photosensitizing capabilities, CA has demonstrated potential in biomedical applications, particularly in the treatment of neoplastic diseases. As an example, water-soluble CA derivatives have been used to generate so-called reactive oxygen species [23] showing promise as anticancer agents in selective tumour targeting [24].

The C_{5v} point-group symmetry [6, 25–28] and a permanent molecular dipole moment of *ca.* 2.1 D [29, 30] lead to a rather unique arrangement of neighboring CA molecules in the solid state (See Supplementary Note 1). As shown in Fig. 1, CA molecules in the α-phase can occupy two crystallographically inequivalent sites, hereafter denoted as A and B. Inversion symmetry gives rise to a distinct tetrameric (centrosymmetric) cluster that is primarily stabilised through C-H$\cdots\pi$ interactions between A–B moieties [31]. In these A–B dimers, the peripheral protons from one CA molecule seek the electron-rich area of its neighbour, and all four CA molecules are connected to each other in a cyclic manner via this structural motif. Less directional van-der-Waals interactions between these tetrameric clusters ultimately lead

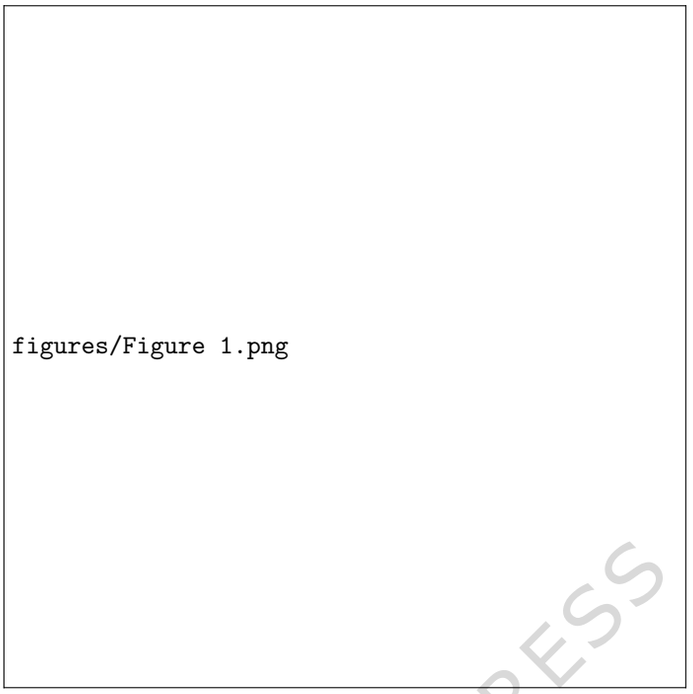

Fig. 1 Tetrameric unit in the α-phase of CA. A and B molecules are shown with different colours and i denotes the center of inversion.

to the observed supramolecular packing in the solid state. Supplementary Figure 1 evinces the presence of well-defined layers on the crystallographic (200) plane with a nearest-neighbour distance of 10.1 Å. These layers are more loosely bound along the perpendicular direction, with a longer spacing of *ca.* 12.9 Å along the *a*-axis.

Given the paucity of experimental data on CA to date, previous works have begun exploring this fascinating molecular system and how its properties may be related to its curved nature [32–34]. To this end, perylene ($C_{20}H_{12}$, hereafter PE) can be regarded as the flat (nearly isobaric, within 1%) counterpart of CA, where a change from a central hexagon to a pentagon leads to a well-defined curvature. Muon spectroscopy and gas-sorption techniques [34] have provided insights into the way CA interacts with atomic (H) and molecular hydrogen (H_2). At liquid-nitrogen temperatures, H_2 was found to diffuse into the crystal lattice, leading to a molar storage capacity of up to one H_2 molecule per unit cell at a pressure as low as 4.6 bar. While still relatively modest, this gas-storage capacity is considerably higher than that observed for its fullerene relative C_{60}. Moreover, the observation of long-lived muonium-adduct radicals highlighted a strong propensity for hydrogenation. The motional narrowing seen in the muon data above 400 K also hinted at the activation of molecular motions within the solid. These results called for a more detailed investigation of CA as a function of temperature [33]. Neutron spectroscopy unequivocally identified correlated stochastic dynamics well within the solid, connected to the suppression of molecular and supramolecular order. As shown in Supplementary Note 2, these relaxation processes

are entirely absent in PE, further indicating that molecular curvature plays a key role in dictating thermophysical response. Moreover, cooling CA from the liquid is accompanied by a strong hysteresis of *ca.* 80 K associated with a deep-supercooled phase as well as with the presence of a dynamically disordered solid phase. These results are in line with a strong temperature dependence of low-energy librations [35]. The complex phenomenology observed to date for CA is in stark contrast with solid PE, which does not exhibit stochastic motions and behaves as a canonical solid with a well-defined vibrational density of states up to the melting point. Fast Scanning Calorimetry (FSC) [32] has enabled the access to previously unknown disordered and ordered phases of CA when using ultrafast heating and cooling rates of at least hundreds of K s^{-1}. As hinted by the neutron data, the planar and highly symmetric structure of PE is also reflected in a high propensity to crystallise even at the highest cooling rates accessible with state-the-art FSC instrumentation. All in all, these results were not anticipated for such seemingly simple molecular systems like CA and PE, particularly in view of what is known about other fullerene adducts [36] and other flat PAHs [2–5].

Motivated by the above, the work presented herein explores the metastable phases of CA well away from thermodynamic equilibrium. To this end, we make use of state-of-the-art FSC to map its thermophysical response at extreme cooling and heating rates. In the first instance, these conditions circumvent crystallisation entirely and allow access to a fully glassy state and to a deeply SuperCooled Liquid (SCL). The annealing of these disordered phases upon heating reveals new polymorphs above ambient temperature. In parallel, we apply Single-Crystal Synchrotron Diffraction (SCSD) over a wide temperature range, to build a microscopic picture of the underlying mechanisms of amorphisation and subsequent crystallisation into hitherto unknown polymorphs.

2 Results

2.1 Glass formation & kinetics of crystallisation

Our first attempts to study CA with FSC techniques had already hinted at the existence of hitherto unexplored metastable phases [32]. A key outcome of this work was the realization that the intrinsic curvature of CA induces a deep supercooled regime and the formation of an amorphous (glassy) phase when the melt is cooled at rates exceeding *ca.* 500 K s^{-1}. This behaviour differs sharply with that of PE, for which crystallisation could not be suppressed even at the highest accessible cooling rates, and thermal hysteresis between melting and recrystallisation is at least one order of magnitude smaller.

Further insights into the transformation of the SCL into the stable and metastable solid phases of CA are shown in Fig. 2a. These FSC data exhibit up to four distinct thermal events over the temperature range 300-500 K. Figure 2b reports two derived quantities from the FSC data: integrated enthalpies, calculated as the sum of the areas of all endothermic and exothermic events within the crystal; and the associated (cooling-rate-dependent) cold-crystallisation temperatures T_{cc}. When CA is cooled at rates above or equal to a Critical Cooling Rate (CCR) of 500 K s^{-1}, the heating scans show five distinct thermal features: a glass-to-liquid transition around 330 K; a

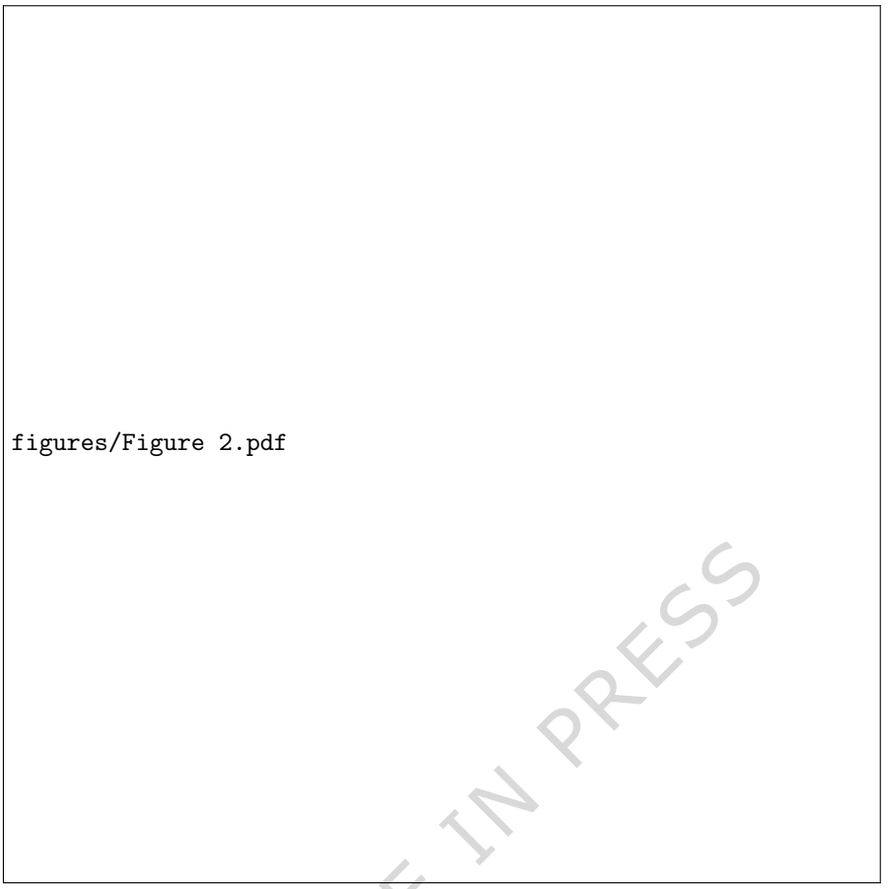

Fig. 2 FSC heating response of CA after cooling from the melt. (a) Heating curves at 1000 K s^{-1}, after cooling at rates of 10-5000 K s^{-1} – see legend. (b) Cooling-rate dependence of the enthalpies and cold-crystallisation temperatures T_{cc} – left and right abscissas, respectively. The vertical dashed line indicates the CCR at *ca.* 500 K s^{-1}, as described in the main text.

cold-crystallisation peak in the range 360-400 K; two crystalline rearrangements, the first one exothermic at *ca.* 440 K and a second one endothermic at *ca.* 490 K; and melting at 543 K. Cooling at rates below the CCR inevitably leads to crystallisation, as previously observed via Differential Scanning Calorimetry (DSC) [33]. By decreasing the cooling rate, all thermal events except melting gradually disappear. As a result, integrated enthalpies at decreasing cooling rates increase from about 4 kJ mol^{-1} up to 17 kJ mol^{-1}. This latter figure corresponds to the enthalpy of melting of CA [37]. Moreover, the temperature of the cold-crystallisation peak shown in Fig. 2b reaches a maximum at a cooling rate of 1000 K s^{-1}. As recent theoretical considerations suggest [38], this non-monotonic (re-entrant) behaviour could emerge from two competing effects involving glass relaxation and nucleation kinetics.

To explore further the crystallisation kinetics in the glassy region, crystallisation of the SCL was avoided by crash-cooling the sample from the melt at 563 K to 323

Fig. 3 Thermal response of CA after vitrification at different rates. Top: FSC scans after cooling from 563 K to 323 K at a rate of 2000 K s^{-1}. The cooling rates shown in the figure correspond to cooling from 323 K to 183 K, followed by heating to 563 K at a constant rate of 1000 K s^{-1}. Bottom: resulting kinetic phase diagram. For further details, see the main text

K at a fixed rate of 2000 K s^{-1}. Following this first step, CA was further cooled at different rates ranging from 1 to 2000 K s^{-1}. The heating scans at a rate of 1000 K s^{-1} after this two-step cooling protocol are shown in the top panel of Fig. 3. At first glance, similar features stand out relative to the data shown in Fig. 2*a*: a maximum in the cold-crystallisation peak temperature when CA is cooled at *ca.* 1000 K s^{-1}; and, at lower cooling rates, the gradual disappearance of intermediate thermal events associated with crystallisation. The bottom panel of Fig. 3 shows the resulting kinetic phase diagram, where the heating scans at 1000 K s^{-1} are represented as a function of temperature and cooling rate. In this contour plot, endothermic(exothermic) events

Fig. 4 Temperature dependence of lattice parameters. Circles correspond to a and c (left ordinate). Diamonds correspond to b and β (right ordinate). Data at 203 K are from the work of Hanson and Nordman [8]. Solid lines are guides to the eye.

are shown in blue(red), respectively. Amorphous CA exists in the glassy state up to temperatures in the range 320-330 K, where a kinetic glass transition is observed. Above T_g, the SCL persists over a narrow temperature range up to the onset of cold crystallisation, as evidenced by a strong exothermic peak in the range 350-390 K. The position of this feature depends quite strongly on cooling rate. Further heating leads to a second solid-to-solid exothermic event at about 430-450 K (T_{ss1}), followed by a less-intense endothermic feature at about 500 K (T_{ss2}). For cooling rates between 500 and 3 K s^{-1}, semi-crystalline CA exists below T_{cc}. The amorphous fraction decreases with decreasing cooling rate. Also, the second exothermic event is shifted to lower temperatures (420-430 K), while the endothermic feature at around 495 K vanishes. When cooling below T_g at rates below 3 K s^{-1}, all molecules crystallise and no further thermal events are observed up to the melting point.

2.2 Structure and its temperature evolution

The powder-diffraction data reported in previous works [33] did not indicate significant variations in long-range order with temperature, an observation in line with available single-crystal diffraction data at 203 and 293 K [8]. Nonetheless, the aforementioned data evinced a progressive increase of weighted profile residuals above room temperature, suggestive of the onset of systematic departures from the low-temperature structure. The rich phenomenology observed with FSC called for a more detailed investigation of these effects using SCSD. The resulting lattice parameters between 200 and 500 K are presented in Fig. 4. All follow a similar and non-trivial trend as a function of temperature, characterized by a sudden increase around the observed glass-transition temperature. The effect seems to be most pronounced along c, followed by the a- and b-axes. These data indicate two different regimes above and below *ca.* 330 K. From a crystallographic perspective, however, it is important to note that the overall lattice symmetry remains unaltered.

An initial structural solution was obtained in the $P2_1/c$ space group with two non-equivalent molecules A and B forming the tetramer shown in Fig. 1. This structure is equivalent to the structure reported previously at 203 K [8]. At room temperature and above, however, difference-Fourier-map analysis shows additional electron density in originally empty regions, located in between the carbon hexagons of molecule A and in areas between the rim-carbons – see Supplementary Figure 4. This density can be accounted for by considering the presence of two distinct orientations of a given molecule, related to each other by a rotation of *ca.* $\pi/5$ about the pentagonal axis. This change in molecular orientation corresponds to half a jump between equivalent positions, with a split occupancy of unity. Such a type of orientational disorder is typical of plastic crystals [39]. It is important to note that this rotation about the high-symmetry axis of CA does not disrupt the overall symmetry of the crystal. Similarly, molecule B also displays extra electron density in between empty regions, although

these only become discernible above 375 K. In the case of B molecules, the rotation is (on average) closer to a 1/3 jump between equivalent positions rather than 1/2. The standard and rotated configurations of A(B) molecule will be hereafter referred to as $A_0(B_0)$ and $A_+(B_+)$, respectively. On the basis of the above, CA molecules were distributed across these two possible sites in the ensuing analysis, adding rigid-body constraints preceding the refinement of their fractional occupancy and coordinates. A detailed account of these results is deferred to the Discussion in the next section.

The marked increase in the ccupancy of (+) sites above the glass transition can be probed further via closer inspection of the Atomic Displacement Parameters (ADPs) obtained from the SCSD data, particularly those corresponding to the carbons on the rims covalently bound to the edge hydrogens. Figure 5 displays the mean values calculated from the equivalent isotropic (thermal) ellipsoid parameters of these carbons, defined as one-third of the trace of the orthogonalized U_{ij} tensor. There is a sharp increase with an onset at around the glass-transition temperature. The behaviour of both A and B molecules is quite similar. As shown by the inset in this figure, thermal disorder takes place primarily perpendicular to the molecular C_{5v} axis. These results are consistent with the observation of stochastic relaxation pathways over this temperature range [33]. Furthermore, the SCSD data provide compelling evidence that such activation of site disorder involves rigid-body rotations of the entire CA molecule about its natural axis of rotation.

3 Discussion

3.1 A microscopic model of disorder in solid corannulene

The FSC data provide incontestable evidence that CA can undergo vitrification just above ambient conditions, well below its melting point. This temperature range coincides with the onset of significant departures from the known structure at lower temperatures, as evinced by the sudden jump in unit-cell parameters immediately above the glass transition – see Fig. 4. Further evidence to this effect is given by the concomitant increase with temperature of the populations of A_+ and B_+ species in the lattice and their associated thermal ellipsoids, as presented in the previous section. The former observables can be used to determine the equilibrium constant between ground and rotated states in solid CA via the van´t Hoff relation

$$\ln\frac{[X_+]}{[X_0]} = -\frac{\Delta G_X}{RT} \ , \tag{1}$$

where X can be either A or B, and ΔG_X is the associated change in the Gibbs free energy $\Delta G_X = \Delta H_X - T\Delta S_X$. Supplementary Figure 5 shows that this expression can be used to describe the experimental data satisfactorily, both in terms of entropic and enthalpic contributions. In the latter case, ΔH_A=7.7±0.3 kJ mol^{-1} and ΔH_B=9.2±0.5 kJ mol^{-1}, that is, A molecules have to surmount an enthalpic barrier that is about 20% lower and, therefore, exhibit a significantly higher propensity to occupy (+) sites at lower temperatures. The entropic contributions to the free energy amount to $\Delta S_A/R$=1.15±0.10 and $\Delta S_B/R$=0.38±0.15. For the case of A, there is a sizeable (positive) entropic gain upon the activation of A_+ sites, indicating that their

activation is favoured quite significantly relative to B. These considerations are in line with the sudden increase in unit-cell volume shown in the top panel of Fig. 6. On the basis of these observations, it appears as if these structural (entropy-favoured) changes in solid CA are primarily driven by A molecules. In the case of B, the entropy change is about three times lower than A, consistent with the observed (smaller) extent of rotation. These differences also indicate that the onset of cooperative effects involving the prior and sequential activation of rotationally excited species ought to be at play for the case of B.

The equilibrium constants also enable us to examine the evolution of A_+ and B_+ fractional occupancies with temperature, as shown in the bottom panel of Fig. 6. For reference, this figure indicates the position of both glass transition and melting point, along with extrapolations at the latter using the fit results discussed in Supplementary Note 5. On purely probabilistic grounds, the fractional occupancy or probability P_+ of populating A_+ or B_+ sites can be subdivided into monomer and dimer contributions within a given tetramer. The associated probabilities assuming that a given site is randomly populated are given by $P_+(1-P_+)$ and P_+P_+ for monomer and dimer populations, respectively – see Fig. 6. Around the glass transition and up to temperatures around the jump in unit-cell volume, the activation of A_+ monomers dominates the scene. At higher temperatures, B_+ becomes increasingly more visible and its fractional occupancy follows rather closely the presence of A_+ dimers. These observations provide compelling evidence that the activation of B_+ sites requires the formation of A_+ dimers within a given tetramer, leading to changes in the surrounding energy landscape that then enable the activation of B. Moreover, the presence of B_+ dimers is negligible even at temperatures reaching the melting point. This transition between the activation of singly occupied $A_+A_0B_0B_0$ and triply occupied $A_+A_+B_+B_0$ tetramers at the higher temperatures is echoed by the further increase in unit-cell volume seen in the SCSD data above 440-450 K. At these temperatures, the overall fractional populations of the latter start becoming comparable to those of the former. In either case, the expansion of the solid follows a sequence of well-defined steps associated with an enhanced swelling of the tetramer units as a result of rotational activation, first of A_+ and then of B_+ sites – *i.e.,* the onset of cooperativity across A and B ensembles. Topologically speaking, this mechanism of activation can be traced back to the structure of the tetramer shown in Fig. 1. The two A molecules lean toward the centre, acting as a separator between the two B molecules. The former(latter) may then be viewed as the core(caps) of the cluster. Both A molecules interact with a given B molecule, either as the electrophile or the nucleophile within a given AB dimer.

The lattice parameters reported in Fig. 4 provide further clues about how the rotational activation of A and B affects supramolecular structure, shown schematically in Supplementary Figure 1. Over the range 300-350 K, the *c*-axis undergoes the strongest (anomalous) expansion, amounting to *ca.* 1.2 %. The *a*-axis follows with *ca.* 0.4 %, whereas expansion along *b* is far less pronounced. Figures S1*c* and S1*d* help us visualize the effects of an increase of A_+. The activated tetramer denoted as a grey ball in these figures has undergone an overall expansion relative to the ground-state tetramer. Such expansion pushes the four nearest neighbours preferentially along the *c*-axis. Next-nearest neighbours along the *b*-axis are far less affected. Likewise, the interaction

with adjacent tetramer planes leads to a measurable (albeit less pronounced) expansion along the *a*-axis, where we can identify an additional two nearest neighbours. These structural considerations can be used to rationalize the sudden (cooperative) increase in unit-cell volume as the glass-transition temperature is crossed from below. As shown in Fig. 6, the fractional population of A_+ at the glass transition corresponds to *ca.* 0.16±0.02, arising from single A_+ excitations within a given tetramer. For N=6 nearest neighbours, the percolation threshold resulting in a network of connected A_+-excited tetramers is approximately given by $1/N = 0.17$, in very good agreement with the SCSD results. In the vicinity of the glass transition, the picture that therefore emerges is that of a CA solid 'decorated' by a dynamically fluctuating and interconnected network of singly occupied A_+ tetramers, resulting in an overall macroscopic expansion of the material.

From the trends shown in the bottom panel of Fig. 6, similar considerations seem to be at play for single B_+ excitations as the melting point is approached, with an (admittedly extrapolated) fractional occupancy of 0.16±0.03. In this scenario, melting would be related to the approach of the same percolation threshold by triply excited $A_+A_+B_+B_0$ tetramers. Using the fractional occupancy data, one can then define an associated order parameter in terms of the emergence of these tetramers, given by

$$\eta = 1 - \frac{[B_+]}{[B_+]_M} \tag{2}$$

where the subscript M refers to the value at melting. This quantity provides a measure of the fraction of the crystal still not containing B_+ species. Figure 7 shows that as melting is approached, η defined in this manner conforms to a Landau-Ginzburg expression of the form

$$\eta^2 = \alpha \left[1 - \frac{T}{T_c}\right] \tag{3}$$

with $T_c/T_m = 0.98\pm0.03$. This result nicely confirms the order-disorder character of the transformation from solid to liquid CA. It also corroborates the validity and usefulness of the order parameter defined via Eq. (2). Within a mean-field picture, the characteristic energy of the underlying interactions amounts to $2RT_c = 9.0\pm0.3$ kJ mol^{-1}, a figure to be compared with ΔH_B=9.2±0.5 kJ mol^{-1}, the enthalpy of activation inferred independently from the temperature dependence of the equilibrium constant. With the benefit of hindsight, our previous DSC studies [32] had already signalled a markedly asymmetric melting peak when heating from below, with readily measurable heat signals as much as 10 K below the reported melting point [41]. These observations constitute strong indicators of a markedly continuous (second-order) character of the solid-to-liquid phase transformation in CA.

3.2 Emergence of polymorphism in corannulene

The distinct and rather peculiar behaviour of CA above the glass transition presented in the last section represents a subtle case of solid-state polymorphism whereby the overall space-group symmetry of the crystal is preserved, yet, at the same time, there are substantial differences between the low- and high-temperature structures of what

had been classed to date as the α-phase. Such is the case even when examining the temporally and spatially averaged observables amenable to scrutiny with SCSD or other crystallographic techniques. On the basis of our results, it is therefore tempting to use the glass-transition temperature to underline a distinction below and above – that is, CA can sustain a 'proper' α-phase as well as a second α'-phase, respectively. From an operational viewpoint, this differentiation serves as a reminder that the former may be seen as a 'canonical crystal,' whereas this is hardly the case for the latter.

Beyond the α- and α'-phases, the kinetic phase diagram reported in Fig. 3 contains a wealth of information on how kinetic arrest may be effected in CA, as well as how it evolves with temperature as it enters and then leaves its glassy state. The enthalpies and transition temperatures for the various thermal events derived from these data are displayed in Fig. 8. We recall that this kinetic phase diagram was obtained by cooling from the liquid to the glass transition, followed by further cooling well into the glassy state at varying cooling rates. As shown in Fig. 8 and summarised in Table 1, it is possible to identify three different solid phases in addition to the glass, SCL, and normal liquid. This result alone is sufficient to establish that other CA polymorphs are now within reach for further scrutiny.

Table 1 Average temperatures (K) and enthalpies (kJ mol^{-1}). Values have been calculated from the data reported in Fig. 8.

T_{cc}	T_{ss1}	T_{ss2}	T_m
378.4±7.7	432.3±6.9	496.7±1.4	542.0±0.8
$-\Delta H_{cc}$	$-\Delta H_{ss1}$	ΔH_{ss2}	ΔH_m
9.4±1.3	2.2±1.2	0.9±0.5	17.0±0.5

Cooling rates into the glassy state above 10 K s^{-1} are sufficient to follow the sequential transformation from the glass into SCL and then into the three aforementioned solid phases. For the magnitudes of the enthalpies shown in Fig. 8, there is a clear hierarchy obeying the order ΔH_m, $-\Delta H_{cc}$, $-\Delta H_{ss1}$, and ΔH_{ss2}, where positive enthalpies denote endothermic events. As the highest cooling rates are approached, $\Delta H_{cc}+\Delta H_{ss1}$ converge to the value of ΔH_m when differences in the heat capacities of solid and liquid CA are taken into account – see Supplementary Note 3. From an energetic viewpoint, this correspondence indicates that the glassy state may be regarded as a representative snapshot of the liquid state. With these thermophysical data at hand, the striking correspondence found between the structural changes discussed in Section 3.1 and the location of the glass transition and T_{cc} can also be scrutized further. The FSC data supports the view that the SCL just above the glass can sustain a substantial amount of tetrameric CA units, which then assemble cooperatively at T_{cc}. Likewise, the SCSD data shown in Figs. 5 and 6 tell us that rotational disorder in the solid emerges cooperatively at the glass transition and persists up to melting

in the form of rotationally activated A and B molecules. We are, therefore, in a situation whereby there are two distinct length scales at play associated with intra- and intercluster configurations. In this case, the magnitude of ΔH_{cc} indicates that upon crossing T_{cc}, CA attains the supramolecular structure shown in Fig. S1, albeit with a degree of intra-cluster rotational disorder distinctly different from that found at ambient conditions. The structural data in Fig. 5 also suggest that the sudden increase in ADPs observed at this temperature might be the actual trigger of cold crystallisation. Further intra-cluster rearrangements would occur upon further heating, as evidenced by the lower magnitude of ΔH_{ss1} (about four times lower than ΔH_{cc}) and associated with the formation of the second polymorph. Given the exothermic nature of this process, this transition would correspond to the opening of previously inaccessible tetramer de-excitation channels. At higher temperatures, the last transformation preceding melting becomes endothermic, with an absolute value of ΔH_{ss2} which is less than half of ΔH_{ss1}. Interestingly, ΔH_{ss2} mirrors that of the liquid and exhibits a clear maximum. Its range of existence is also the narrowest, requiring the highest-attainable cooling rates. These observations suggest that the second solid phase of CA has overrelaxed relative to the α'-phase and that, as melting is approached from below, intra-cluster excitations can bring the solid back to thermodynamic equilibrium.

4 Conclusions

State-of-the-art FSC and SCSD have shed new light on the structural and dynamical complexity of CA, whose curved topology enables vitrification. For this seemingly simple geodesic polyarene, the phenomenology observed via FSC is immensely rich and unanticipated, including the emergence of polymorphs. The single-crystal diffraction data provide key information on how CA behaves above room temperature and how rotational disorder emerges. In particular, we have observed crystallographic sites associated with rotations about the molecular high-symmetry axis. These sites are thermally active and exhibit cooperative behaviour. Their progressive occupation is linked to the activation of tetramer units in the solid, ultimately leading to melting. Looking ahead, these findings invite further investigation into the properties and behavior of CA, particularly using methodologies and techniques capable of probing dynamical phenomena across different time and length scales. Advanced capabilities developed at synchrotron sources could further enable *in-situ* studies via FSC [42]. The present work also calls for efforts into alternative routes for polymorph stabilization, circumventing the present need for fast cooling and heating rates.

5 Methods

Sample preparation

CA was synthesized using previously reported protocols [43], followed by slow sublimation in vacuum at 443 K to yield a bright-yellow powder. Poly-dimethylsiloxane (PDMS, viscosity 10^5 cP) and diethyl ether were purchased from Sigma Aldrich and used as received. For the SCSD experiments, single crystals of CA were obtained

from slow evaporation in a cyclohexane solution. Suitable crystals for diffraction were selected under a microscope and mounted on the tip of a 0.3 mm glass capillary.

Fast scanning calorimetry

FSC experiments were performed with a Mettler Toledo Flash DSC-1 unit, equipped with a dual-stage intracooler to operate between 183 and 723 K. During all measurements, the chamber was purged with nitrogen gas at a flow rate of 20 mL min^{-1}. Temperature and heat-flow rates were calibrated using the melting transition of Indium. Thermal lags were evaluated by comparing the onset of melting in the FSC unit to that observed with DSC using a Q2000 Calorimeter from TA Instruments. Given the large surface-area-to-volume ratio of the FSC samples, we found that CA above its melting temperature rapidly evaporates, thus preventing further measurements on a given sample. To circumvent these limitations, the specimen was prepared following recently established protocols [32], as better described in Supplementary Note 3. After these procedures, CA was first melted at 563 K in the FSC calorimeter, followed by a cooling ramp down to 183 K at rates ranging from 5000 to 0.1 K s^{-1}. Subsequently, heating scans were performed from 183 to 563 K at 1000 K s^{-1}. The critical cooling rate of CA was identified as the highest cooling rate at which the appearance of a melting endotherm could be observed. To explore crystallisation kinetics in the glassy state, the temperature-cycling protocol first involved a cooling from the melt at 563 K down to 323 K at a rate of 2000 K s^{-1}. This run was followed by a series of cooling runs down to 183 K at variable rates between 2000 and 0.1 K s^{-1}. These cooling runs were linked to each other by a heating scan at 1000 K s^{-1} up to 563 K. The position of either exothermic or endothermic transformations correspond to peak maxima. The only exception is the glass-transition temperature, taken at the half step of the heat flow. Latent heats of crystallisation and melting were calculated via integration of the corresponding C_p curves, taking a two-point baseline between the lower and upper temperatures reported in Supplementary Table 1. Sample masses were calculated via normalization of the melting endotherm with respect to the melting enthalpy previously determined via DSC for a known mass.

Single-crystal synchrotron diffraction

Experiments as function of temperature were conducted on two different crystals. Capillaries were covered by a larger 0.7-mm capillary and sealed in an Argon atmosphere to avoid oxidation at high temperature. All sample handling was carried out in an Argon-filled glove box (<1 ppm O_2 and H_2O). SSCD data were collected on the XRD1 beamline of the Elettra synchrotron light source (Trieste, Italy) using the rotating-crystal method with a Dectris Pilatus 2M area detector and incident wavelengths of 0.6888 and 0.7000 Å. An Oxford Danfysik DGB0002 gas blower was employed over the temperature range 293-470 K, above which the crystal readily sublimes and deposits into a colder region in the capillary. Diffraction data were indexed and integrated using CrysalisPro [44], after masking the shadow of the gas blower, and then analysed using Olex2 [45]. Structures were solved using the ShelXT algorithm with the intrinsic

method [46], while structure refinement was performed using ShelXL [46] – see Supplementary Table 2. For both crystals, we could not find any signs of twinning. The ADPs of all carbon atoms were refined anisotropically, whereas hydrogen atoms were placed at the calculated positions and refined with restrained isotropic parameters. More details are provided in Supplementary Note 4.

Data Availability

The X-ray crystallographic coordinates for structures reported in this Article have been deposited at the Cambridge Crystallographic Data Centre (CCDC), under deposition number CCDC 2477280-2477266. These data can be obtained free of charge from The Cambridge Crystallographic Data Centre via www.ccdc.cam.ac.uk/data_request/cif. Numerical source data for graphs and charts can be accessed at https://doi.org/10.17605/OSF.IO/X9TRB. Other data generated or analysed during this study are available from the corresponding authors upon reasonable request.

Acknowledgements

Financial support for this work has been secured through Grants TED2021-129457B-I00 funded by MCIN/AEI/10.13039/501100011033 and the European Union NextGenerationEU/PRTR; and PID2023-146442NB-I00 funded by MCIU. We also thank UK Research & Innovation for providing neutron beam time on the IRIS beamline at the ISIS Facility – experiment RB2510476. We acknowledge Elettra Sincrotrone Trieste for beam access, Giorgio Bais for support during the SCSD experiments, and Dan George Dumitrescu for useful discussions on crystallographic analysis. We gratefully acknowledge the continued financial support received from the IKUR Strategy under the collaboration agreement between Ikerbasque Foundation and the Materials Physics Center, on behalf of the Department of Science, Universities & Innovation of the Basque Government.

Author contributions

Investigation, formal analysis, data curation: M.G, V.D.L, B.B., J.S, F.F-A; Supervision: D.C., F.F-A; Writing, review, editing: M.G, V.D.L, D.C., F.F-A; Funding acquisition: F.F-A.

Declarations

The authors declare no competing interests.

References

[1] Dunitz, J. D. & Bernstein, J. Disappearing Polymorphs. *Accounts of Chemical Research* **28**, 193–200 (1995). URL https://pubs.acs.org/doi/abs/10.1021/ar00052a005.

[2] Pick, A. *et al.* Polymorph-Selective Preparation and Structural Characterization of Perylene Single Crystals. *Crystal Growth Design* **15**, 5495–5504 (2015). URL https://pubs.acs.org/doi/10.1021/acs.cgd.5b01130.

[3] Botoshansky, M., Herbstein, F. H. & Kapon, M. Towards a complete description of a polymorphic crystal: The example of perylene redetermination of the structures of the (z = 2 and 4) polymorphs. *Helvetica Chimica Acta* **86**, 1113–1128 (2003).

[4] Potticary, J. *et al.* An unforeseen polymorph of coronene by the application of magnetic fields during crystal growth. *Nature Communications* **7**, 1–7 (2016).

[5] Mattheus, C. C. *et al.* Identification of polymorphs of pentacene. *Synthetic Metals* **138**, 475–481 (2003).

[6] Tsefrikas, V. M. & Scott, L. T. Geodesic polyarenes by flash vacuum pyrolysis. *Chemical Reviews* **106**, 4868–4884 (2006). URL https://doi.org/10.1021/cr050553y.

[7] Merz, L. *et al.* Polymorph selection in 2D crystals by phase transition blocking. *Chemical Communications* 5871–5873 (2009).

[8] Hanson, J. C. & Nordman, C. E. The crystal and molecular structure of corannulene, C20H10. *Acta Crystallographica Section B Structural Crystallography and Crystal Chemistry* **32**, 1147–1153 (1976). URL http://scripts.iucr.org/cgi-bin/paper?S0567740876012430.

[9] Grabowsky, S. *et al.* Electron Density of Corannulene from Synchrotron Data at 12 K, Comparison with Fullerenes. *Zeitschrift für Naturforschung B* **65**, 452–460 (2010). URL https://www.degruyter.com/view/j/znb.2010.65.issue-4/znb-2010-0403/znb-2010-0403.xml.

[10] Ayalon, A., Rabinovitz, M., Cheng, P.-C. & Scott, L. T. Corannulene Tetraanion: A Novel Species with Concentric Anionic Rings. *Angewandte Chemie International Edition in English* **31**, 1636–1637 (1992). URL http://doi.wiley.com/10.1002/anie.199216361.

[11] Yamabe, T., Yahara, K., Kato, T. & Yoshizawa, K. Vibronic Coupling and JahnTeller Effects in Negatively Charged Corannulene. *The Journal of Physical Chemistry A* **104**, 589–595 (2000). URL http://pubs.acs.org/doi/abs/10.1021/jp992496g.

[12] Dubois, D. *et al.* Spectroelectrochemical study of the C60 and C70 fullerenes and their mono-, di-, tri- and tetraanions. *Journal of the American Chemical Society* **113**, 4364–4366 (1991). URL http://pubs.acs.org/doi/abs/10.1021/ja00011a069.

[13] A Main Group Metal Sandwich: Five Lithium Cations Jammed Between Two Corannulene Tetraanion Decks. *Science* **333**, 1008–1011 (2011). URL http://www.sciencemag.org/cgi/doi/10.1126/science.1208686.

[14] Zabula, A. V., Spisak, S. N., Filatov, A. S., Grigoryants, V. M. & Petrukhina, M. A. How charging corannulene with one and two electrons affects its geometry and aggregation with sodium and potassium cations. *Chemistry - A European Journal* **18**, 6476–6484 (2012).

[15] Zabula, A. V. & Petrukhina, M. A. in *Structural Perspective on Aggregation of Alkali Metal Ions with Charged Planar and Curved Carbon π-Surfaces* 1 edn, Vol. 61 375–462 (Elsevier Inc., 2013). URL http://dx.doi.org/10.1016/B978-0-12-407692-1.00003-5http://linkinghub.elsevier.com/retrieve/pii/B9780124076921000035https://linkinghub.elsevier.com/retrieve/pii/B978012407692100003 5.

[16] Clamshell Opening in the Mixed-Metal Supramolecular Aggregates Formed by Fourfold Reduced Corannulene for Maximizing Intercalated Metal Content. *Angewandte Chemie International Edition* **53**, 140–145 (2014). URL http://doi.wiley.com/10.1002/anie.201308090.

[17] Spisak, S. N. *et al.* Convex and Concave Encapsulation of Multiple Potassium Ions by Sumanenyl Anions. *Journal of the American Chemical Society* 150804112047002 (2015). URL http://pubs.acs.org/doi/abs/10.1021/jacs.5b06662.

[18] Filatov, A. S. *et al.* Self-assembly of tetrareduced corannulene with mixed Li–Rb clusters: dynamic transformations, unique structures and record 7 Li NMR shifts. *Chem. Sci.* **6**, 1959–1966 (2015). URL http://xlink.rsc.org/?DOI=C4SC03485F.

[19] Banerjee, S., Pillai, C. & Majumder, C. Hydrogen absorption behavior of doped corannulene: A first principles study. *International Journal of Hydrogen Energy* **36**, 4976–4983 (2011). URL http://linkinghub.elsevier.com/retrieve/pii/S0360319911000140.

[20] Bauert, T. *et al.* Quadruple anionic buckybowls by solid-state chemistry of corannulene and cesium. *Journal of the American Chemical Society* **135**, 12857–12860 (2013).

[21] Rellan-Pineiro, M. *et al.* DFT and MP2 study of the interaction between corannulene and alkali cations. *Journal of Molecular Modeling* **19**, 2049–2055 (2013). URL http://link.springer.com/10.1007/s00894-012-1632-8.

[22] Li, X. *et al.* Comparative analysis of biological effect of corannulene and graphene on developmental and sleep/wake profile of zebrafish larvae. *Acta Biomaterialia* **55**, 271–282 (2017).

[23] Cai, C. *et al.* A water-soluble corannulene with highly efficient ROS production. *Materials Chemistry and Physics* **281**, 125885 (2022). URL https://doi.org/10.1016/j.matchemphys.2022.125885.

[24] An Unrevealed Molecular Function of Corannulene Buckybowl Glycoconjugates in Selective Tumor Annihilation by Targeting the Cancer-Specific Warburg Effect. *Advanced Science* **9**, 1–15 (2022).

[25] Barth, W. E. & Lawton, R. G. Synthesis of corannulene. *Journal of the American Chemical Society* **93**, 1730–1745 (1971). URL http://pubs.acs.org/doi/abs/10.1021/ja00736a028.

[26] Georgakilas, V., Perman, J. A., Tucek, J. & Zboril, R. Broad family of carbon nanoallotropes: Classification, chemistry, and applications of fullerenes, carbon dots, nanotubes, graphene, nanodiamonds, and combined structures. *Chemical Reviews* **115**, 4744–4822 (2015). URL https://doi.org/10.1021/cr500304f.

[27] Li, X., Kang, F. & Inagaki, M. Buckybowls: Corannulene and its derivatives. *Small* **12**, 3206–3223 (2016). URL https://doi.org/10.1002/smll.201503950.

[28] Nestoros, E. & Stuparu, M. C. Corannulene: a molecular bowl of carbon with multifaceted properties and diverse applications. *Chemical Communications* **54**, 6503–6519 (2018). URL https://doi.org/10.1039/c8cc02179a.

[29] Lovas, F. J. *et al.* Interstellar chemistry: A strategy for detecting polycyclic aromatic hydrocarbons in space. *Journal of the American Chemical Society* **127**, 4345–4349 (2005).

[30] Martin, J. W. *et al.* The polarization of polycyclic aromatic hydrocarbons curved by pentagon incorporation: The role of the flexoelectric dipole. *The Journal of Physical Chemistry C* **121**, 27154–27163 (2017). URL https://doi.org/10.1021/acs.jpcc.7b09044.

[31] Sanyal, S., Manna, A. K. & Pati, S. K. Functional Corannulene: Diverse Structures, Enhanced Charge Transport, and Tunable Optoelectronic Properties. *ChemPhysChem* **15**, 885–893 (2014). URL https://onlinelibrary.wiley.com/doi/10.1002/cphc.201301050.

[32] Di Lisio, V. *et al.* Fast scanning calorimetry on volatile carbon-based materials. *Thermochimica Acta* **719**, 179414 (2023). URL https://doi.org/10.1016/j.tca.2022.179414https://linkinghub.elsevier.com/retrieve/pii/S0040603122002672.

[33] Gaboardi, M., Silverwood, I., Braunewell, B., Siegel, J. & Fernandez-Alonso, F. Emergence of dynamical disorder and phase metastability in carbon nanobowls. *Carbon* **183**, 196–204 (2021). URL https://www.sciencedirect.com/science/article/pii/S0008622321006813.

[34] Gaboardi, M. *et al.* The interaction of hydrogen with corannulene, a promising new platform for energy storage. *Carbon* **155**, 432–437 (2019). URL https://doi.org/10.1016/j.carbon.2019.08.087.

[35] Le Parc, R. *et al.* New insights on vibrational dynamics of corannulene. *Journal of Physical Chemistry C* **116**, 25089–25096 (2012). URL http://pubs.acs.org/doi/abs/10.1021/jp307536dpapers://dc5b7a66-c191-4125-90d3-2536c98d4438/Paper/p17935.

[36] Armstrong, J., Mukhopadhyay, S., Bresme, F. & Fernandez-Alonso, F. Heads or tails: how do chemically substituted fullerenes melt? *Phys. Chem. Chem. Phys.* **18**, 17202–17209 (2016). URL http://dx.doi.org/10.1039/C6CP01333Chttp://xlink.rsc.org/?DOI=C6CP01333C.

[37] Acree, W. & Chickos, J. S. Phase Transition Enthalpy Measurements of Organic and Organometallic Compounds. Sublimation, Vaporization and Fusion Enthalpies From 1880 to 2010. *Journal of Physical and Chemical Reference Data* **39**, 1880–2002 (2010).

[38] Schmelzer, J. W. P., Tropin, T. V. & Schick, C. Effects of structural relaxation of glass-forming melts on the overall crystallization kinetics in cooling and heating. *Entropy* **25** (2023). URL https://www.mdpi.com/1099-4300/25/11/1485.

[39] Fischer, J. E. & Heiney, P. A. Order and disorder in fullerene and fulleride solids. *Journal of Physics and Chemistry of Solids* **54**, 1725–1757 (1993).

[40] Petrukhina, M. A., Andreini, K. W., Mack, J. & Scott, L. T. X-ray Quality Geometries of Geodesic Polyarenes from Theoretical Calculations: What Levels of Theory Are Reliable? *The Journal of Organic Chemistry* **70**, 5713–5716 (2005). URL http://pubs.acs.org/doi/abs/10.1021/jo050233e.

[41] The enthalpy of vaporization and sublimation of corannulene, coronene, and perylene at T= 298.15 K. *The Journal of Chemical Thermodynamics* **34**, 1195–1206 (2002). URL http://linkinghub.elsevier.com/retrieve/pii/S002196140200229Xhttp://linkinghub.elsevier.com/retrieve/pii/S0021961402909778.

[42] van den Bruinhorst, A. *et al.* Defying decomposition: the curious case of choline chloride$_{SI}$. *Nature Communications***14**, 1 − −7(2023).

[43] Butterfield, A. M., Gilomen, B. & Siegel, J. S. Kilogram-scale production of corannulene. *Organic Process Research and Development* **16**, 664–676 (2012).

[44] (2014), A. Crysalispro. *Agilent Technologies, Yarnton, England* **Version 1.171.37.35**.

[45] Dolomanov, O. V., Bourhis, L. J., Gildea, R. J., Howard, J. A. K. & Puschmann, H. OLEX2 : a complete structure solution, refinement and analysis program. *Journal of Applied Crystallography* **42**, 339–341 (2009). URL https://scripts.iucr.org/cgi-bin/paper?S0021889808042726.

[46] Sheldrick, G. M. Crystal structure refinement with SHELXL. *Acta Crystallographica Section C Structural Chemistry* **71**, 3–8 (2015). URL https://scripts.iucr.org/cgi-bin/paper?S2053229614024218.

Fig. 5 Temperature dependence of isotropic ADPs. Left ordinate axis: ADPs for the rim carbons. Solid lines are guides to the eye. Right ordinate axis, dashed lines: rate of variation of these parameters with temperature. The data at 203 K are from the work of Petrukhina *et al.* [40]. The blue-shaded region corresponds to the temperature range where cold crystallisation is observed via FSC. The dashed line indicates the position of the glass transition. Graphical inset: A_0 (blue) and A_+ (yellow) states at 413 K, viewed along the C_{5v}-axis. Thermal ellipsoids correspond to a 25% probability level. To facilitate visualization, only the average positions of the hydrogen atoms have been displayed.

Fig. 6 Temperature evolution of unit-cell volume and fractional populations. Top: unit-cell volume, obtained from the data in Fig. 4. Bottom: fractional populations of A_+ (black) and B_+ (red) sites. Thick solid lines and error bars have been obtained from the fits of the data shown in Supplementary Figure 5. Solid and dashed lines indicate predicted populations of (+) species – see legend. For reference, the position of the glass transition and melting point are shown by vertical dashed lines.

Fig. 7 Temperature dependence of the order parameter. Black circles have been obtained from the SCSD data and the dashed solid line corresponds to a fit to Eq. (3). The square corresponds to the critical temperature T_c derived from the fit. The associated error represents a 2σ confidence level. The vertical dotted line indicates the temperature of melting [41].

Fig. 8 Cooling-rate dependence of enthalpies and transition temperatures. Enthalpies (top) and transition temperatures (bottom) as a function of the cooling rate, using the FSC data of Fig. 3. Average values of these data are reported in Table 1.

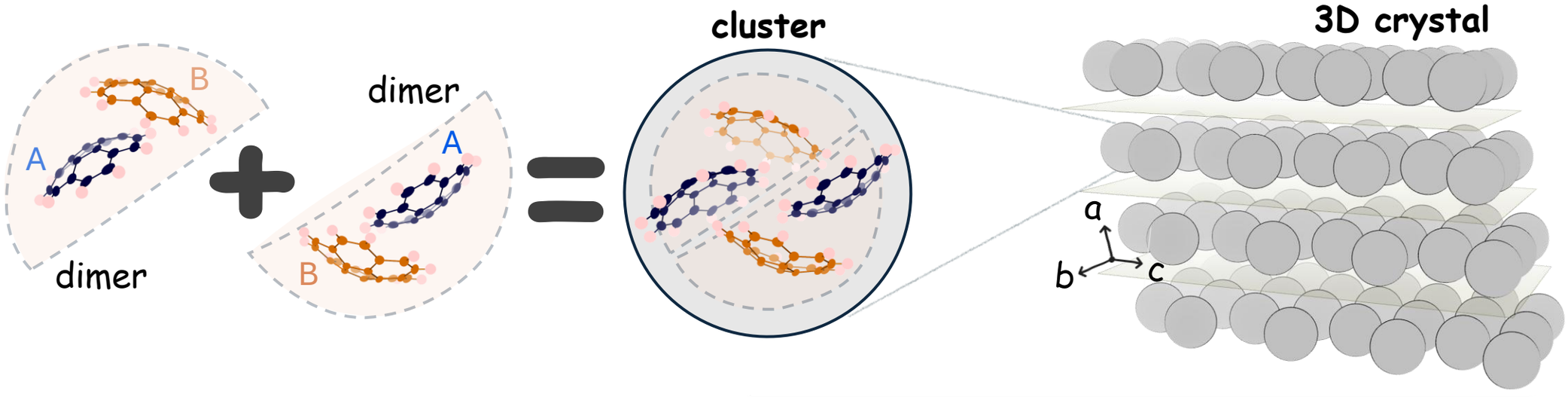

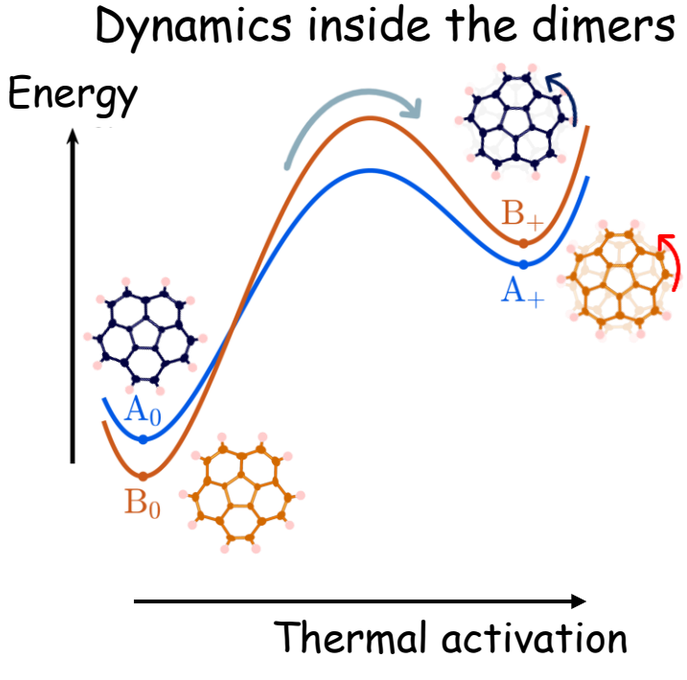

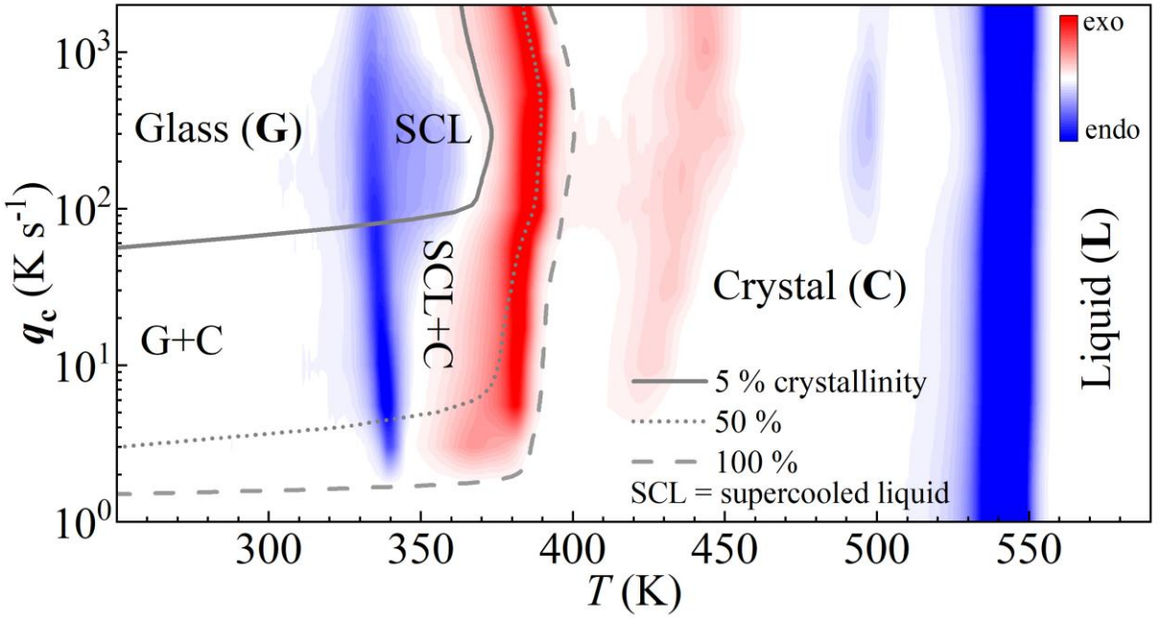

thermally-excited clusters → Large supercooling gap & glassy state → Polymorphism

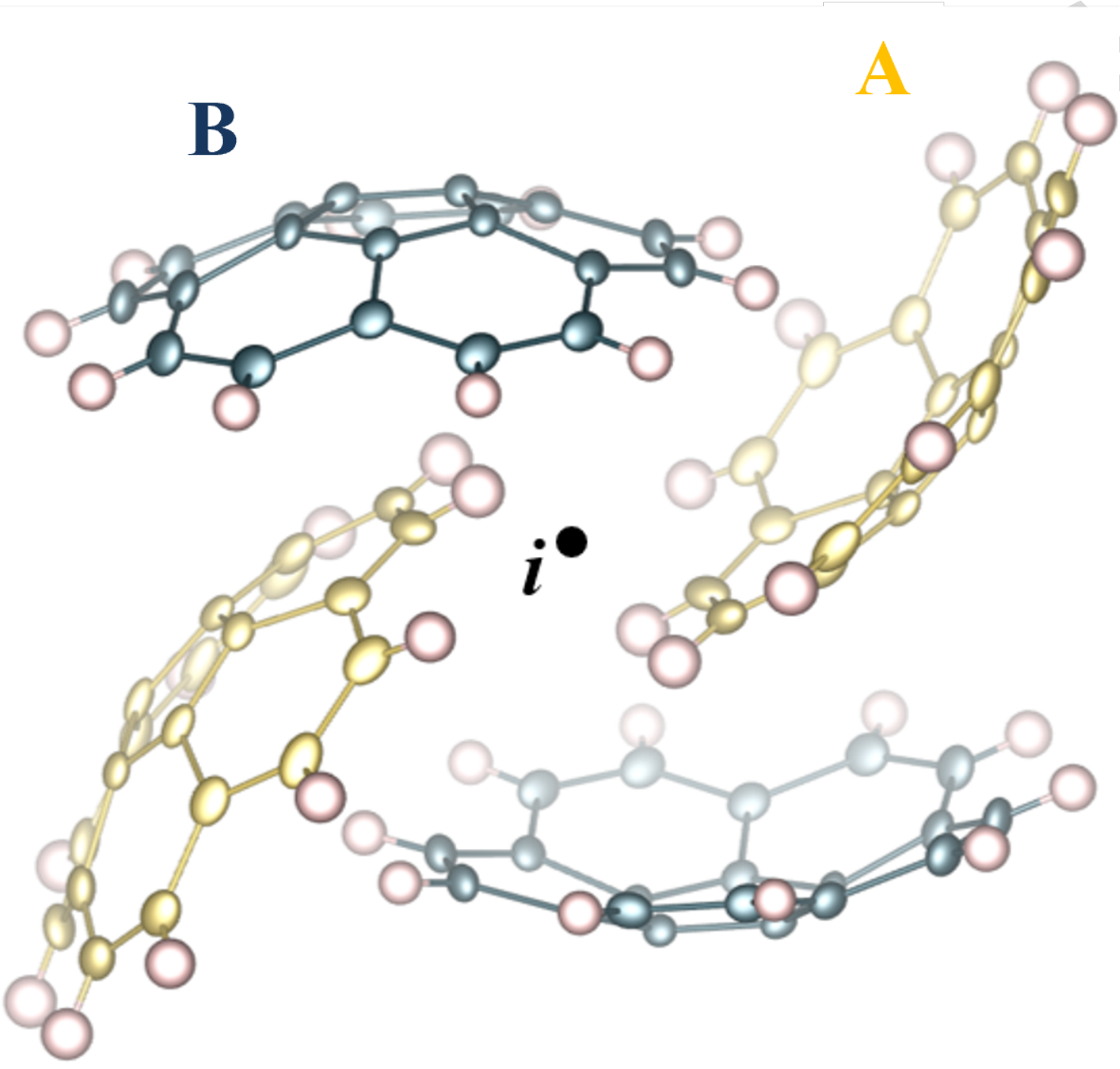

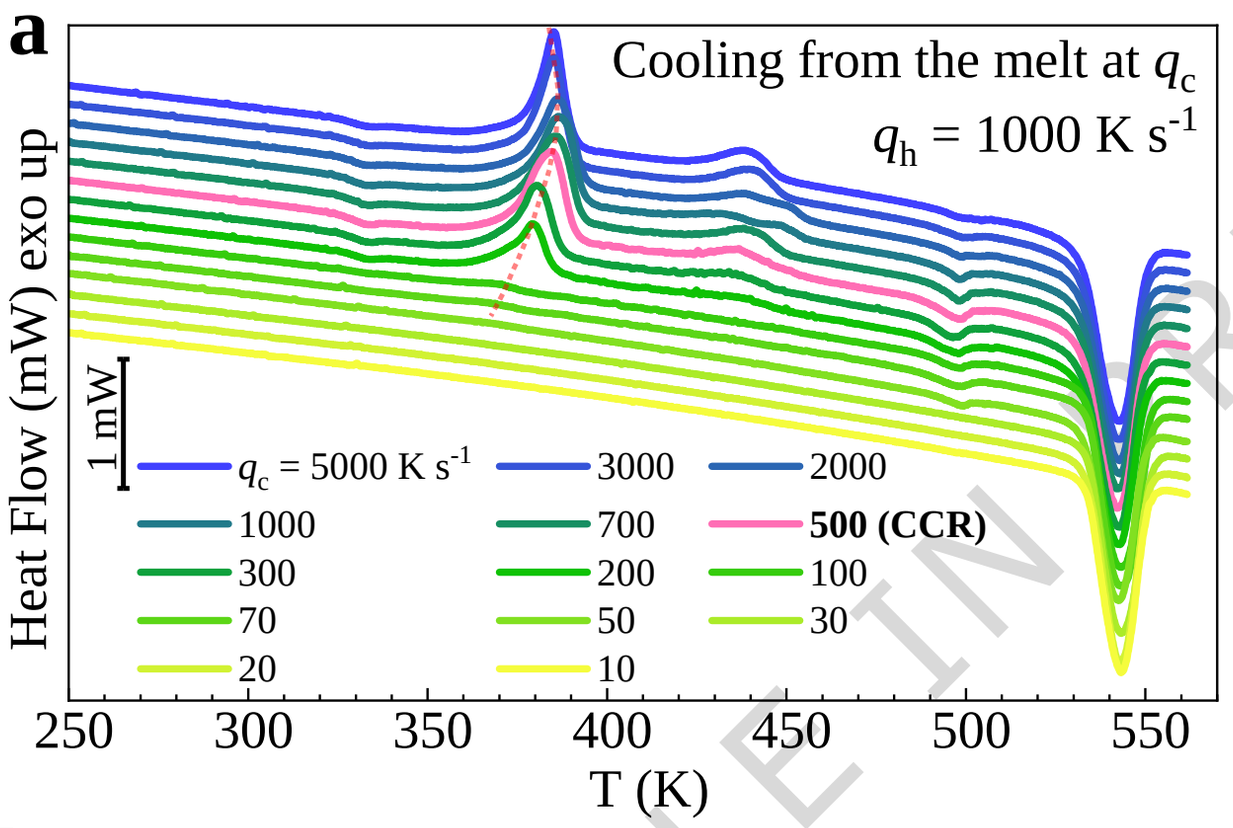

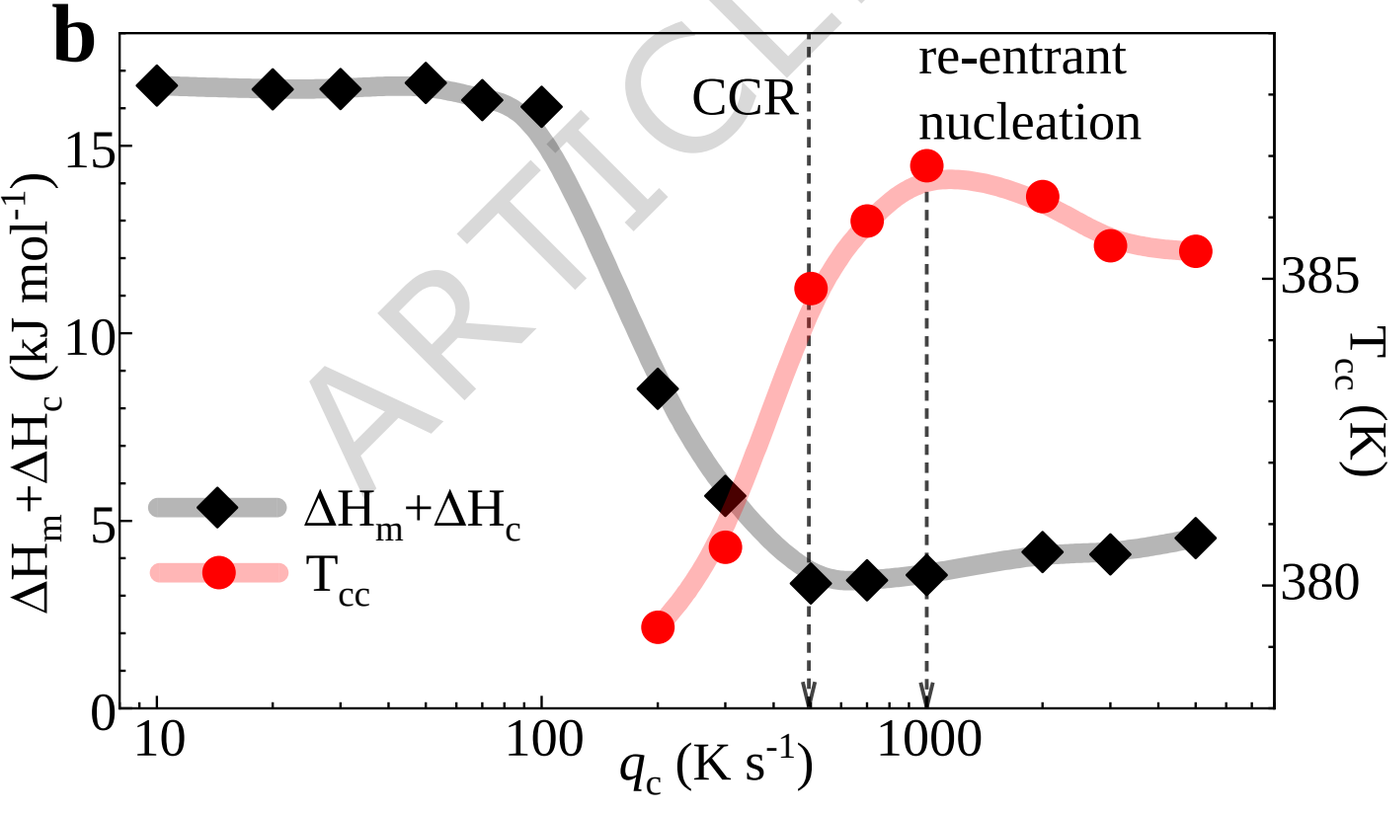

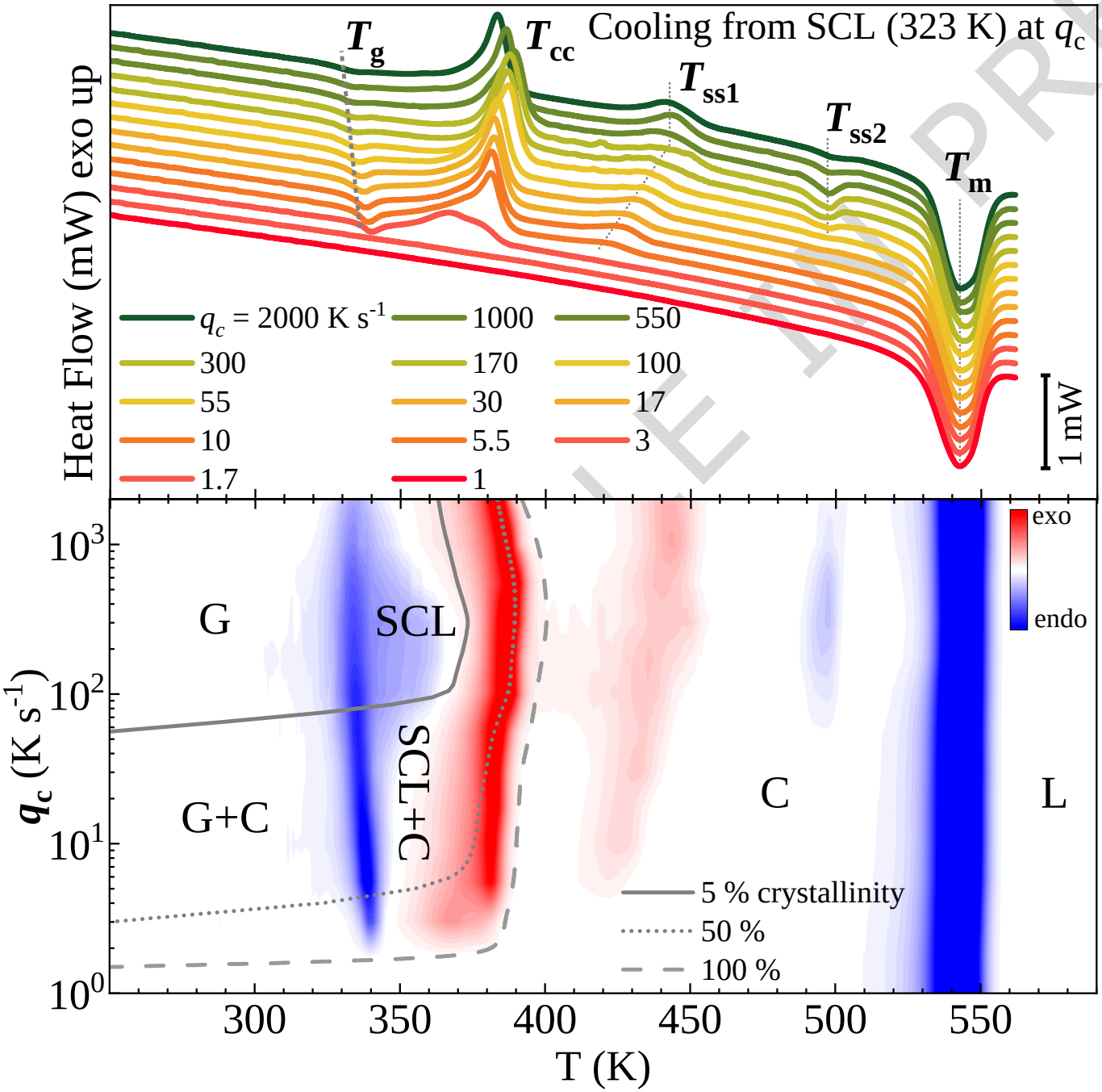

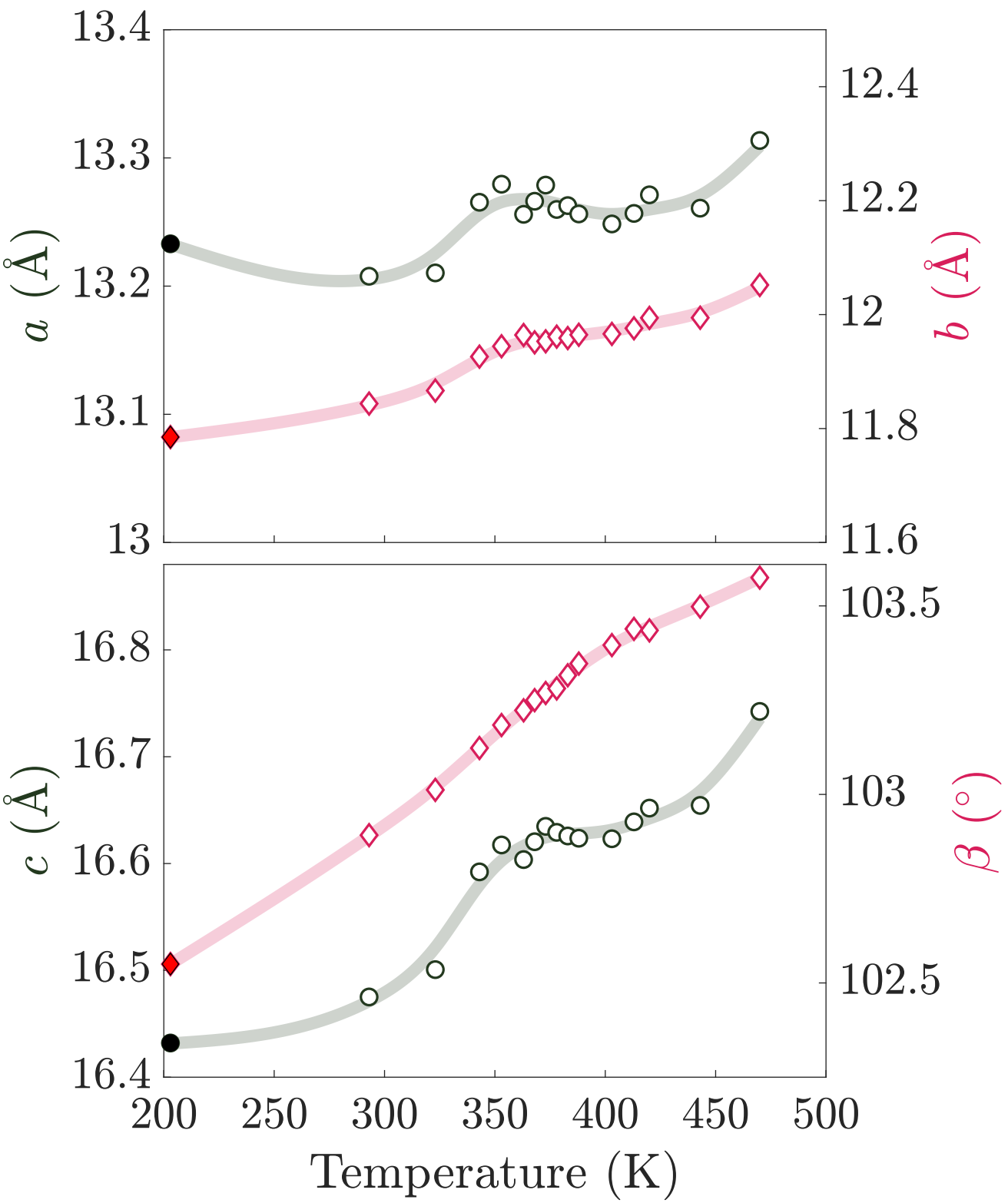
13.4
13.3
13.2
13.1
13
a (Å)
12.4
12.2
12
11.8
11.6
b (Å)
16.8
16.7
16.6
16.5
16.4
c (Å)
103.5
103
102.5
β (°)
200
250
300
350
400
450
500
Temperature (K)

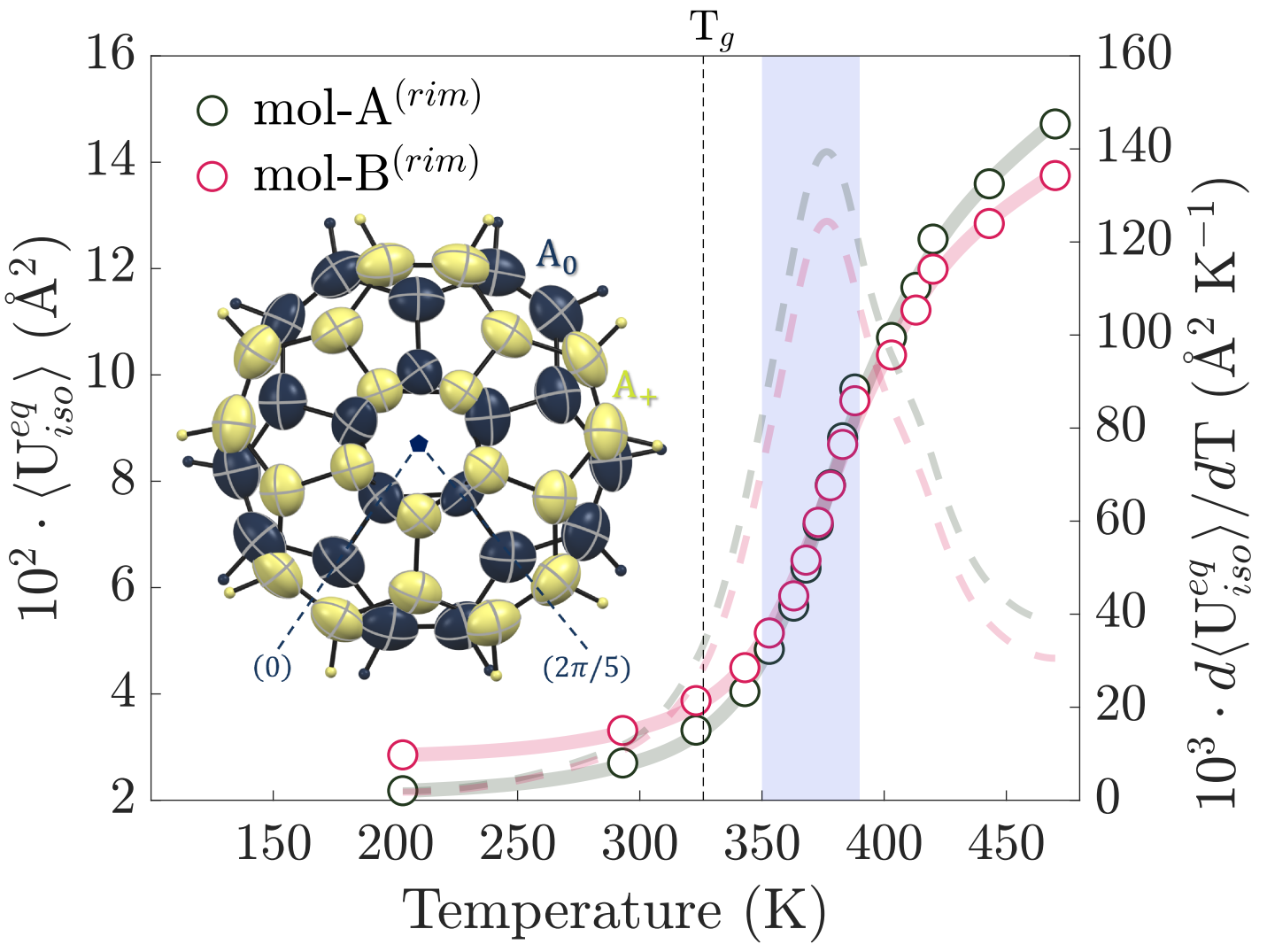
T$_g$
mol-A$^{(rim)}$
mol-B$^{(rim)}$
A$_0$
A$_+$
(0)
(2π/5)
$10^2 \cdot \langle U^{eq}_{iso} \rangle$ (Å^2)
$10^3 \cdot d\langle U^{eq}_{iso} \rangle / dT$ (Å^2 K^{-1})
Temperature (K)
2
4
6
8
10
12
14
16
0
20
40
60
80
100
120
140
160
150
200
250
300
350
400
450

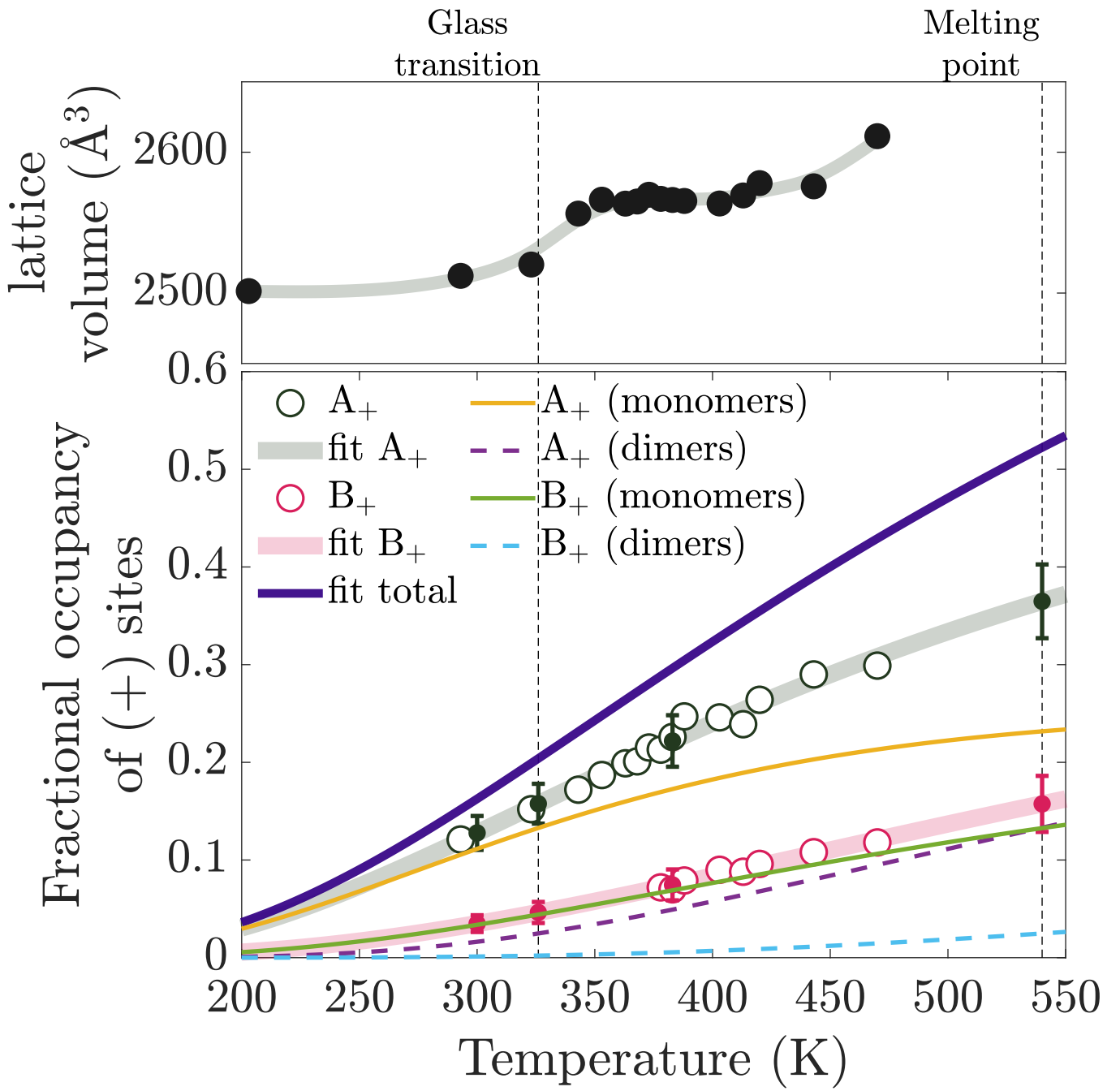
Glass transition
Melting point
lattice volume (Å^3)
2600
2500
0.6
0.5
0.4
0.3
0.2
0.1
0
Fractional occupancy of (+) sites
A$_+$
fit A$_+$
B$_+$
fit B$_+$
fit total
A$_+$ (monomers)
A$_+$ (dimers)
B$_+$ (monomers)
B$_+$ (dimers)
200
250
300
350
400
450
500
550
Temperature (K)

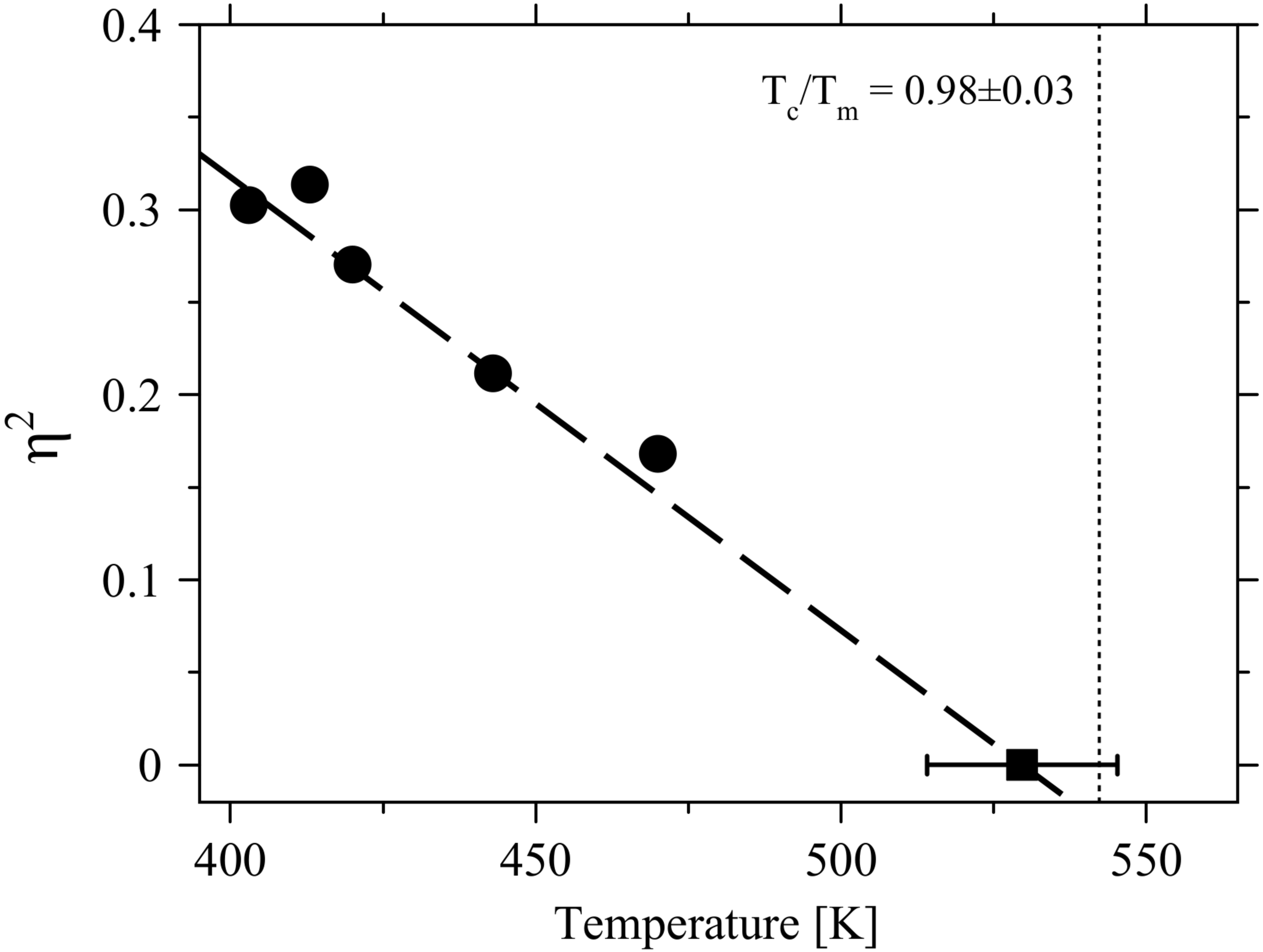
$T_c/T_m = 0.98 \pm 0.03$
η^2
0.4
0.3
0.2
0.1
0
400
450
500
550
Temperature [K]

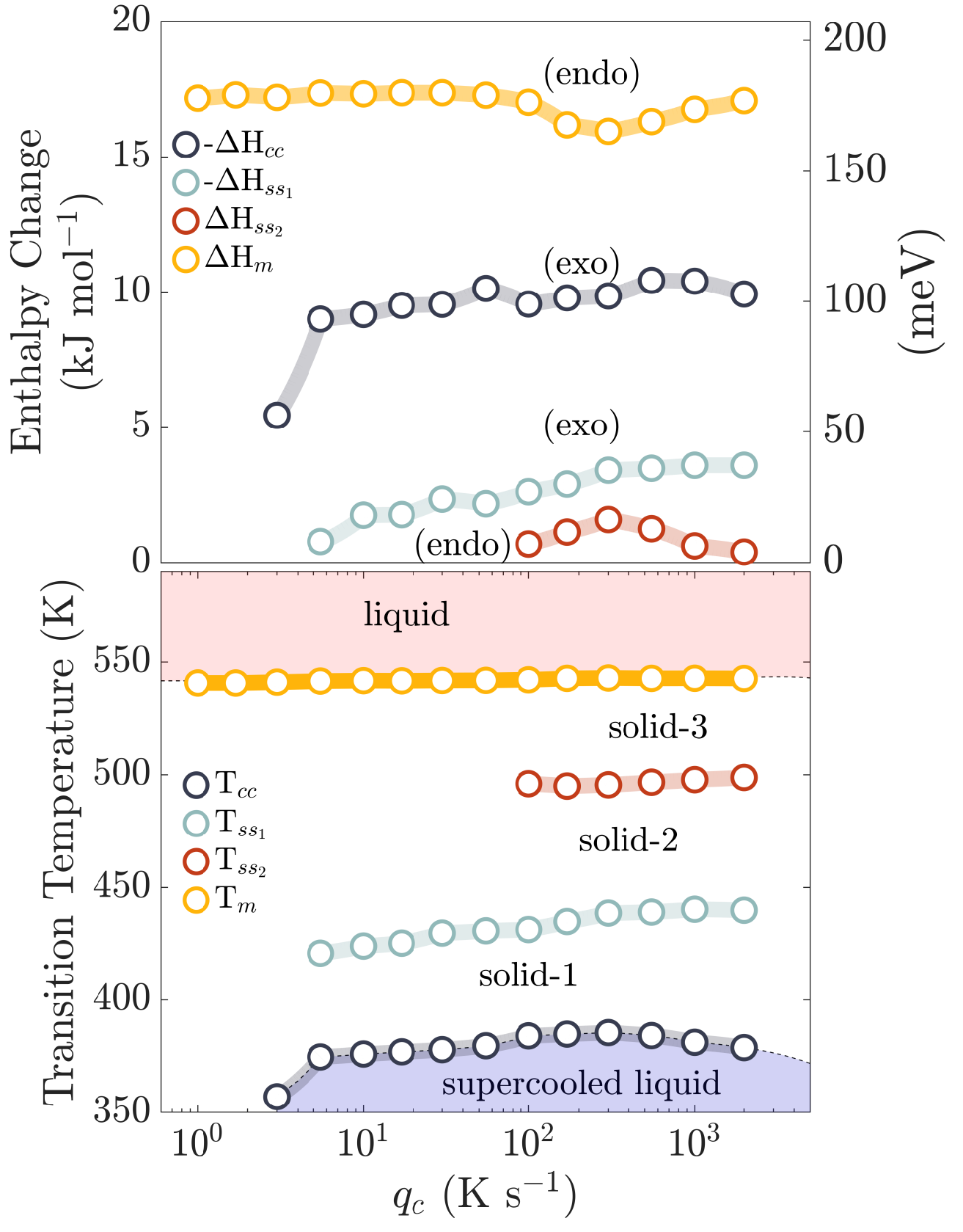
Enthalpy Change (kJ mol^{-1})
(meV)
20
15
10
5
0
200
150
100
50
0
(endo)
(exo)
(exo)
(endo)
-ΔH$_{cc}$
-ΔH$_{ss_1}$
ΔH$_{ss_2}$
ΔH$_m$
Transition Temperature (K)
550
500
450
400
350
liquid
solid-3
solid-2
solid-1
supercooled liquid
T$_{cc}$
T$_{ss_1}$
T$_{ss_2}$
T$_m$
10^0
10^1
10^2
10^3
q_c (K s^{-1})